

Design and performance of an ultra-high-vacuum-compatible artificial channel-cut monochromator

Suresh Narayanan,* Alec Sandy, Deming Shu, Michael Sprung, Curt Preissner and Joseph Sullivan

Advanced Photon Source, Argonne National Laboratory, Argonne, IL 60439, USA.
E-mail: sureshn@aps.anl.gov

The design and performance of a novel ultra-high-vacuum-compatible artificial channel-cut monochromator that has been commissioned at undulator beamline 8-ID-I at the Advanced Photon Source are presented. Details of the mechanical and optical design, control system implementation and performance of the new device are given. The monochromator was designed to meet the challenging stability and optical requirements of the X-ray photon correlation spectroscopy program hosted at this beamline. In particular, the device incorporates a novel in-vacuum sine-bar drive mechanism for the combined pitch motion of the two crystals and a flexure-based high-stiffness weak-link mechanism for fine-tuning the pitch and roll of the second crystal relative to the first crystal. The monochromator delivers an exceptionally uniform and stable beam and thereby improved brilliance preservation.

© 2008 International Union of Crystallography
Printed in Singapore – all rights reserved

Keywords: X-ray monochromator; coherent X-ray scattering; ultra-high vacuum.

1. Introduction

With the advent of several third-generation synchrotron sources, there has been tremendous development in coherence-based experimental tools such as coherent X-ray diffraction (Williams *et al.*, 2003; Pfeifer *et al.*, 2006) and X-ray photon correlation spectroscopy (XPCS) (Falus, Borthwick *et al.*, 2006; Fluerasu *et al.*, 2005; Gutt *et al.*, 2003). In particular, these experiments require monochromatic X-ray beams and are highly brilliance limited. The monochromators used in such beamlines must thereby preserve the beam brilliance by having highly polished diffracting faces. For XPCS experiments, additionally, the monochromator should have very high stability so that spurious monochromator motions do not corrupt the fluctuating scattered X-ray signal arising from the sample. Undulator beamline 8-ID-I, which hosts the XPCS program at the Advanced Photon Source (APS), requires a double-bounce Ge(111)¹ monochromator to produce a monochromatic beam with the appropriate brilliance preservation, stability and longitudinal coherence for XPCS measurements in the small-angle regime (Sandy *et al.*, 1999; Lurio *et al.*, 2000).

2. Motivation

A 'traditional' channel-cut monochromator crystal is a U-shaped channel through a monolithic block of the mono-

chromator material exposing the desired Bragg-reflecting planes on both interior sides of the channel. Advantages are that the diffracting faces are inherently parallel so the mechanical design for the monochromator becomes fairly simple. The disadvantage of a traditional channel-cut design is that the reflecting crystal faces cannot be polished as well as independent crystals, thereby inducing considerable structure in the beam. On the contrary, existing monochromator designs that use two independent crystals have several degrees of freedom for precise alignment of the parallelism of the two crystals. This results in loss of stability owing to insufficiently stiff mechanical stages and couplings and thereby do not fulfill the stringent stability requirements for the above applications.

Fig. 1(a) shows the monochromatic beam produced by the traditional channel-cut monochromator at 8-ID-I as a two-dimensional intensity map measured 5 m downstream of the monochromator using a Roper Scientific CoolSnap CCD detector and Zeiss tube lens system (10× magnification) that yields 0.645 $\mu\text{m pixel}^{-1}$ resolution. Figs. 1(b) and 1(c) show the typical intensity cross sections measured on a PIN diode point detector by scanning a 20 $\mu\text{m} \times 20 \mu\text{m}$ aperture across the beam in the horizontal and vertical directions, respectively. Evidently, the beam incident on the collimating slits that select a coherent fraction of the monochromatic beam is highly non-uniform, varying by more than 50%, leading to decreased optical contrast, decreased XPCS signal-to-noise ratio (Falus, Lurio & Mochrie, 2006) and negative implications for the stability of the overall set-up. The spatial inhomogeneity is attributed to the large surface roughness of the unpolished channel-cut crystal which introduces random and unwanted

¹ Since longitudinal coherence length requirements are less stringent for small-angle X-ray scattering, germanium is used as the monochromator instead of silicon, resulting in a threefold gain in the coherent flux.

phase modulation into the X-ray beam (Wang *et al.*, 2000; Vartanyants & Robinson, 2003). An enhanced ‘Z-step’ design of a channel-cut crystal (Li *et al.*, 2004) also resulted in a spatially inhomogeneous X-ray beam that was statistically indistinguishable from that shown in Figs. 1(a)–1(c).

Motivated by the above, we embarked on a new ‘artificial’ channel-cut monochromator design that facilitates polishing of the diffracting faces while preserving the mechanical stability provided by our traditional channel-cut monochromator. In particular, the device incorporates a novel in-vacuum sine-bar drive mechanism for the combined pitch motion of the two crystals and a flexure-based high-stiffness weak-link mechanism for fine-tuning the pitch and roll of the second crystal relative to the first crystal. The mechanical design is a significant improvement over that for a double multilayer monochromator in which the motions are transmitted through vacuum using bellows (Shu *et al.*, 1995; Ice *et al.*, 2000). The remainder of this paper discusses the design and performance of the artificial channel-cut monochromator and is organized into the following sections: mechanical and vacuum design (§3), X-ray optical design and characterization (§4), control system implementation for the monochromator (§5) and monochromator performance (§6).

3. Mechanical and vacuum design

The new monochromator must meet several demanding mechanical requirements to be suitable for the XPCS experiments that are routinely performed at beamline 8-ID-I.

(i) The monochromator must be compatible with the APS beamline vacuum policy (Davey, 1997) for devices directly coupled to the storage-ring vacuum. In particular, the monochromator must be housed in an ultra-high-vacuum (UHV) enclosure (10^{-9} mbar), and the water-cooling design for the first crystal must be such that there are no direct in-vacuum liquid-coolant joints.

(ii) For stability reasons the two crystals of the monochromator must be mounted on a single UHV-compatible high-stiffness and precision rotary stage. Moreover, the mechanism must allow selection of monochromatic photon energies from 5 to 11 keV, spanning the first harmonic energy spectrum from the APS ‘A’ undulator.

(iii) The second crystal of the monochromator must have independently controllable high-precision and high-stiffness pitch and roll stages to adjust the parallelism of the two crystals.

(iv) The monochromator must be mechanically stable over periods of several days so that it does not introduce spurious fluctuating signals into the XPCS measurements.

Fig. 2 shows a detailed cross-sectional view of the monochromator design that meets the above requirements. Referring to Fig. 2, a precision hollow shaft (1) supported by three sets of ceramic shaft bearings (2) inside a precisely machined rigid housing permits stable angular rotation of the two-crystal assembly by means of the sine-bar mechanism. The sine bar (3) is rigidly mounted to the shaft and has a 13° rotation range ($10\text{--}23^\circ$) that corresponds to an energy range of 5–11 keV

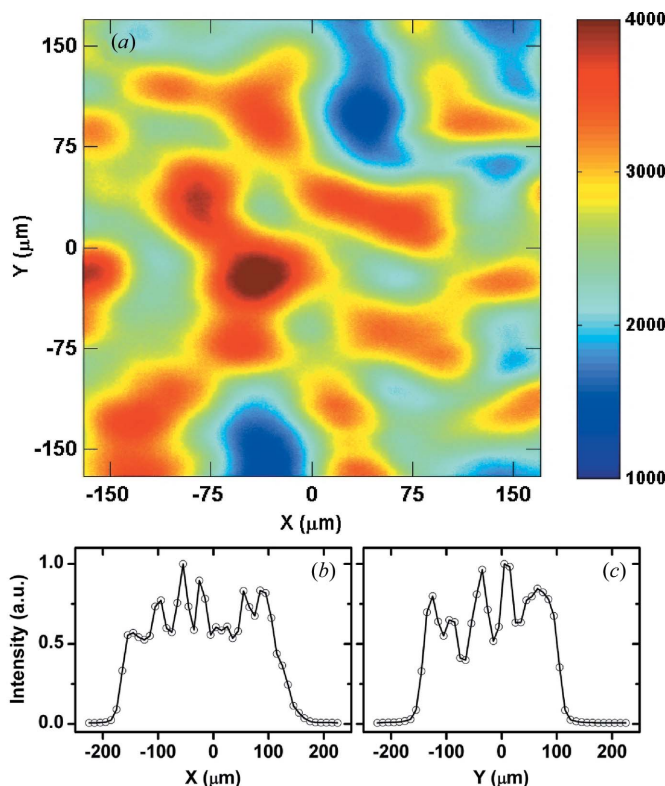


Figure 1 (a) Monochromatic beam from a traditional channel-cut monochromator imaged using an optically coupled CCD detector, showing a highly inhomogeneous intensity distribution. The intensity cross section measured using a $20\ \mu\text{m} \times 20\ \mu\text{m}$ aperture on a PIN diode point detector (b) in the horizontal and (c) in the vertical direction.

using Ge(111) crystals. The long shaft supported at the ends by high-precision bearings provides exceptional stiffness and rigidity to the sine-bar. Using a hardened ruby ball (4) as a precision contact point, the sine-bar arm is coupled to the driving mechanism using a set of anti-backlash springs. The

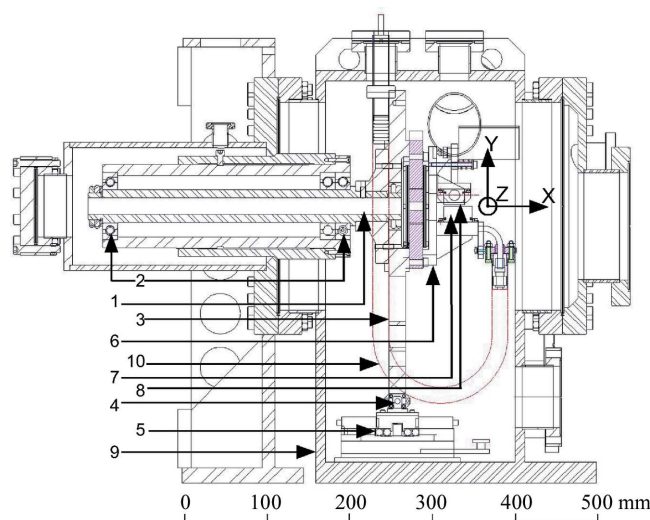


Figure 2 Elevation cross section orthogonal to the X-ray beam direction showing the mechanical design of the artificial channel-cut monochromator. The X-ray beam comes out of the plane of the paper, along the positive Z-direction. Numbered labels are described in the text.

springs provide the restoring force to ensure that the sine bar always stays in contact with the ruby ball when the ball is retracted. The driving mechanism comprises a commercial UHV-compatible ceramic motor linear stage (55 mm travel) (5) that has a 10 nm closed-loop linear resolution based on an UHV-compatible linear grating encoder (Renishaw RGH25) on the stage. This yields exceptionally high angular resolution (~ 50 nrad) in a compact design and is thereby also well suited for use with germanium, silicon and diamond monochromator crystals. The artificial channel-cut crystal mechanism (6), with the first (7) and the second crystal (8), is attached to the front of the sine bar, which is cradled by the high-stiffness precision shaft. The entire assembly, including the channel-cut crystal cage, is contained in a compact UHV chamber (9) eliminating the use of bellows to transmit the motion and thereby any residual vacuum forces. Water cooling is provided using highly flexible stainless-steel formed bellows shrouded by vacuum bellows used under reverse pressure (10). With this design of the water connection, the direct in-vacuum liquid-coolant joints are avoided, eliminating the risk of contaminating the UHV environment. A gravity-feed mechanism was used for the water cooling to minimize the vibrations. The monochromator assembly is mounted on a motorized optical table with two translational and three rotational degrees of freedom (Barraza *et al.*, 1994). The sine-bar and the driving mechanism are shown more clearly in Fig. 3 in the side view of the monochromator. The artificial channel-cut crystal cage is shown in simplified form in order to make clear the sine-bar mechanism.

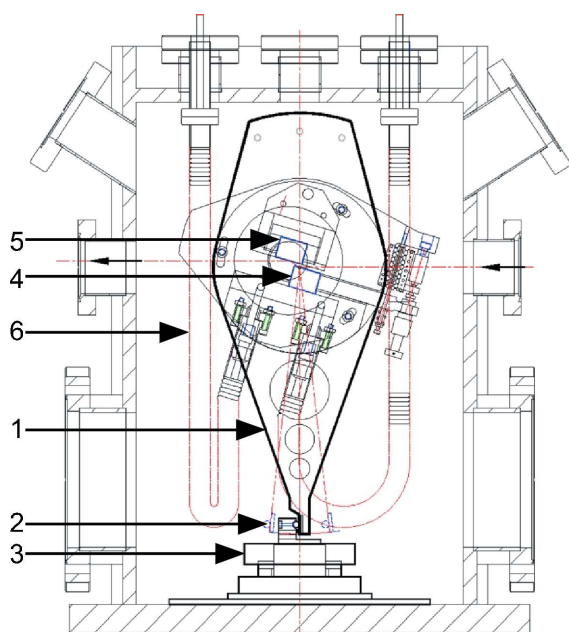


Figure 3
Side view of the monochromator showing the sine-bar and the driving mechanism. The X-ray beam direction is shown by unlabeled arrows. The constituent elements are as follows: sine-bar (1), ruby ball (2), nanomotion driving mechanism (3), first crystal (4), second crystal (5) and vacuum jacket for the water-cooling line (6).

To develop a stable mechanism that facilitates aligning an assembly of two crystals to achieve the same performance as a single channel-cut crystal, we have developed an UHV-compatible version of a novel high-stiffness weak-link mechanism (Shu *et al.*, 2000). The high-stiffness weak-link mechanism consists of three sub-assemblies: one compact sine-bar driving mechanism and two crystal holders, one for each of the two crystals. Test results with a 1 meV bandwidth monochromatic beam show that the angular drift of two crystals attached to each other in this fashion and attributable to the high-stiffness weak-link mechanism is less than 25 nrad h^{-1} (Shu *et al.*, 2003).

Fig. 4 shows the design of the artificial channel-cut crystal cage for the UHV-compatible monochromator. Two sets of stacked thin-metal weak-link modules are used in the driving mechanism: one acting as a pair of rotary bearings (1) for a planar rotary shaft, and the other as a linear stage (2) to support a coupling plate (3) between the picomotor and piezoelectric transducer (PZT) translator. Both weak-link mechanisms have two modules mounted on each side of the base plate (4). The weak-link modules consist of 16 layers of stainless-steel weak-link sheets bonded together with a total thickness of 4 mm. Unlike traditional kinematic linear spring mechanisms, the overconstrained weak-link mechanism provides much higher structure stiffness and stability. Using a laminar structure configured and manufactured by chemical etching and lithography techniques, we are able to design and build a planar-shape high-stiffness high-precision weak-link module. Further details of the weak-link design are described elsewhere (Shu *et al.*, 2007). Special care was taken to minimize any virtual leaks during the bonding process and the modules were tested for UHV after a bake-out at 373 K for 24 h. A base pressure of 2×10^{-10} mbar was attained after

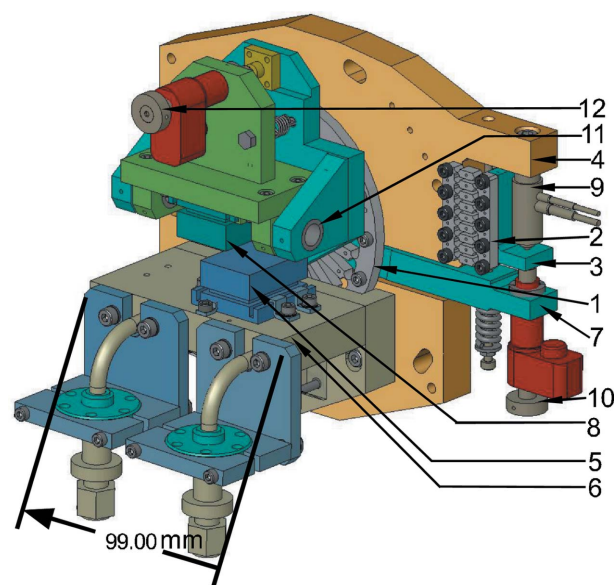


Figure 4
Three-dimensional model of the artificial channel-cut monochromator showing the crystal mounts, water cooling and the weak-link assembly for the second crystal pitch and roll adjustment. Numbered labels are described in the text.

pumping for 24 h and residual gas analysis showed no detectable traces of hydrocarbon contamination.

The first crystal (5) is mounted on a water-cooled crystal holder (6) fixed to the base plate. A compact sine-bar (7) is installed at the center of the planar rotary shaft for the pitch alignment between the second crystal (8) and the first crystal, which is the critical motion of the mechanism. A PZT drive (9) (Physik Instrumente P-841-15 μm travel) is mounted directly on the base plate, and a Picomotor (10) (New Focus 8301-UHV) is directly mounted on the compact sine-bar. Since both the drives have a ball-tip, an interface plate (3) coupled using a pair of high-stiffness linear weak-link modules is used to create a stable interface between the two ball-tip stages. Rough pitch adjustment is performed by the open-loop Picomotor providing 40 nm (300 nrad) resolution, and fine pitch adjustment is performed by the closed-loop-controlled PZT with a strain-gauge sensor providing 4 nm (30 nrad) resolution. Second-crystal roll motion is provided by the combination of a pair of commercial flexure bearings (11), a yoke assembly and a second open-loop Picomotor (12).

4. Optical design and characterization

A relatively small gap of 3 mm was chosen for the artificial channel-cut crystal assembly so as to have a compact mechanical design, a small offset in the monochromatic beam height, and maximum angular range for a given linear travel of the sine bar. The mechanical design allowed an adjustable gap in the range 1–5 mm during assembly of the crystals. The 3 mm gap was preferred over an even smaller gap to minimize the radiated heat load from the first crystal onto the uncooled second crystal. The spatial offset between the incident ‘pink’ and the monochromatic beam is given by $2G\cos\theta$, where G is the gap between the crystal faces. Fig. 5 shows the ray-tracing results at the extremities of the designed energy range, 5 keV and 11 keV. The spatial offset in the beam height over the above energy range is less than 400 μm . The rotation center for the combined pitch motion of the two crystals was positioned on the surface of the first crystal, 5 mm from the edge, so as to cover the above energy range with a single rotational motion.

Ge(111) crystals of dimensions 25 mm \times 25 mm \times 20 mm were fabricated from a Ge(100) ingot. X-ray rocking-curve measurements were carried out on the ingot prior to the fabrication to ensure its perfect crystallinity. After etching, the crystals were successfully polished to state-of-the-art surface finish. Compared with silicon, it is relatively difficult to obtain perfect germanium single crystals, and polishing procedures are not as well established. Nevertheless, optical metrology results showed that the root-mean-square surface roughness was less than 0.1 nm and the optical flatness was better than $\lambda/25$, where $\lambda = 638$ nm. X-ray topography measurements were made after the polishing, using the higher-order Ge(333) reflection, to ensure that the crystals were perfect and devoid of any measurable strain.

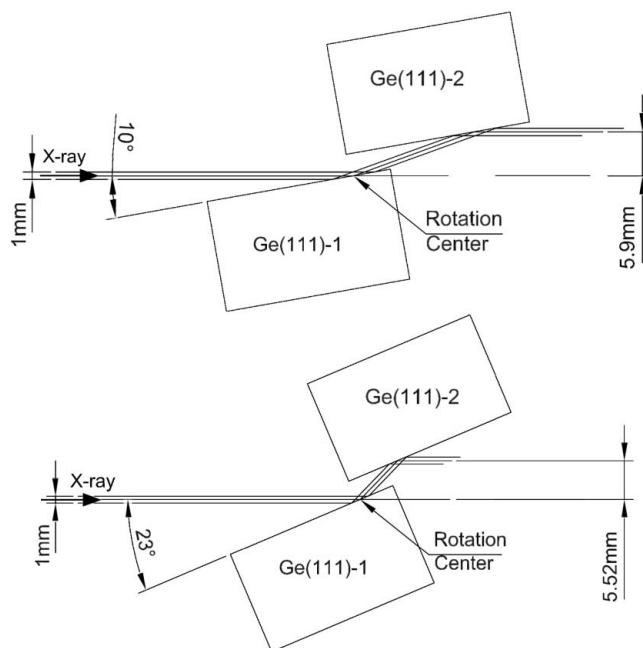


Figure 5

Ray tracing of the artificial channel-cut crystal assembly carried out at the extremities of the designed angular range, 10° (top) and 23° (bottom), corresponding to 11 keV and 5 keV, respectively. Polychromatic ‘pink’ beam is incident from the left and the monochromatic beam is transmitted to the right.

5. Monochromator controls

Achieving the mechanical and vacuum design requirements reported in the previous section required incorporation of several novel UHV-compatible motion stages. The key motion stage among them is an UHV-compatible linear slide assembly comprising a precision crossed-roller bearing slide from Alio Industries, piezoelectric nanomotors (2 \times HR-4) from Nanomotion, a grating encoder (RGH25) from Renishaw, and an Ethernet-based closed-loop four-axis servo controller (SPiiPlus-PCI) with sin/cos interpolation capability from ACS Motion Control. The grating encoder, with a groove spacing of 20 μm when used with sin/cos interpolation (~ 2048) in the ACS motion controller, resulted in a precision of 10 nm (1 encoder count). The combination delivers exceptionally precise closed-loop positioning in vacuum over extended length scales and velocity ranges.

An important additional requirement, therefore, was ensuring that this new assembly could be seamlessly integrated into beamline 8-ID’s VME-based EPICS control system. As illustrated schematically in Fig. 6, this was achieved by the creation of an EPICS 3.14 device driver so that a standard EPICS motor record can communicate over the Ethernet with ACSPL+ command sequences exposed by a socket layer hosted on the ACS Motion SPiiPlus motion controller. Motion programs for absolute positioning, jogging and homing were written and stored in the program buffers on the motion controller. A single buffer was dedicated for each axis of motion so that multiple buffers, which can be executed in parallel, enable simultaneous multi-axis motion. The Ethernet-based architecture also permits ready access to

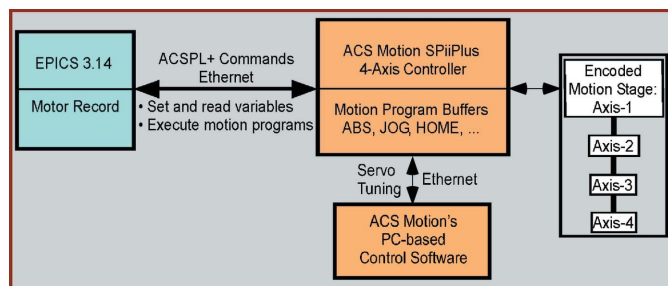


Figure 6 Schematic showing the control system implementation based on Ethernet architecture for driving the primary sine-bar mechanism for the combined pitch motion of the artificial channel-cut crystal assembly.

specialized servo tuning and motion-profile creation using ACS Motion's PC-based application 'Motion Machine Interface' without switching delicate cabling.

The nanomotors in the linear stage for the primary sine-bar have two operating modes: (i) velocity (AC) mode, which is the default mode, and (ii) step (DC) mode. In the AC mode the motors are always under servo control and thereby have very low duty-cycle in vacuum to prevent overheating. In the DC mode the motors function like a piezo actuator, operating under an extremely low applied power to maintain position to within a single encoder count (± 10 nm). The travel range in the DC mode is limited to ± 150 nm but delivers exceptional positional stability to within a single encoder count for an extended period of days. Algorithms were developed using ACSPL+ interfaced to EPICS to switch the nanomotor to the AC mode while scanning and to the DC mode after settling.

6. Monochromator performance

The artificial channel-cut monochromator was installed in beamline 8-ID-I in April 2006. A picture of the complete monochromator assembly is shown elsewhere (Narayanan *et al.*, 2006). Details of the beamline configuration are summarized elsewhere (Sandy *et al.*, 1999), with the relevant change that the monochromator is positioned 65 m downstream of the source. Fig. 7(a) shows the monochromatized beam at 7.35 keV produced by the artificial channel-cut Ge(111) monochromator. Figs. 7(b) and 7(c) show the typical intensity cross sections measured on a PIN diode point detector by scanning a $20 \mu\text{m} \times 20 \mu\text{m}$ aperture across the beam in the horizontal and vertical directions, respectively. Evidently, its intensity profile is significantly more uniform than that produced by the 'traditional' channel-cut monochromator previously installed on beamline 8-ID-I [Figs. 1(a)–(c)]. In particular, the variation in intensity over the beam area is less than 10%. A significant contribution to the intensity variation arises from the broad vertical band in the image and is attributed to imperfections in the side-bounce mirror in the first optics enclosure. This was verified by imaging the beam reflected from the side-bounce mirror without the monochromator crystal in the beam. The horizontal and vertical stripes at the edges of the image are due to Fraunhofer diffraction from the beam-defining slits.

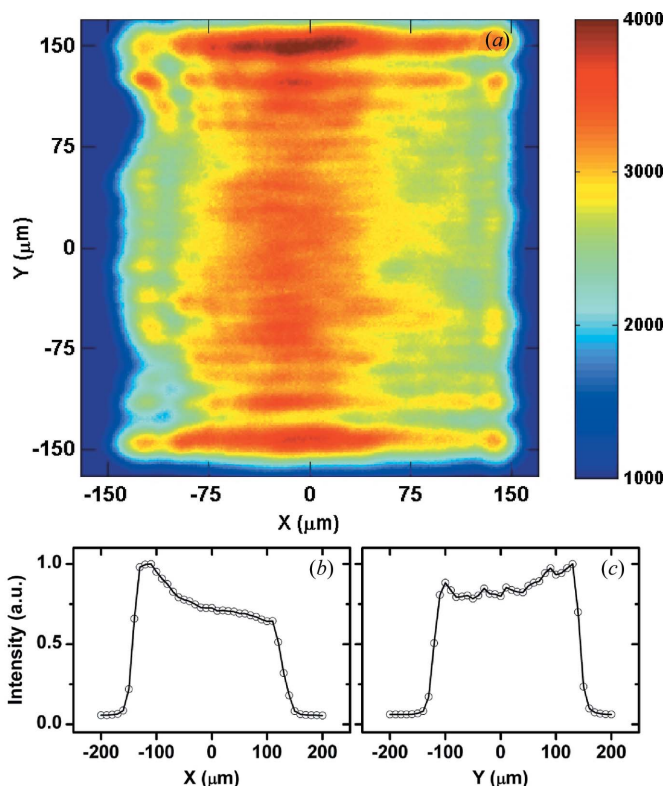
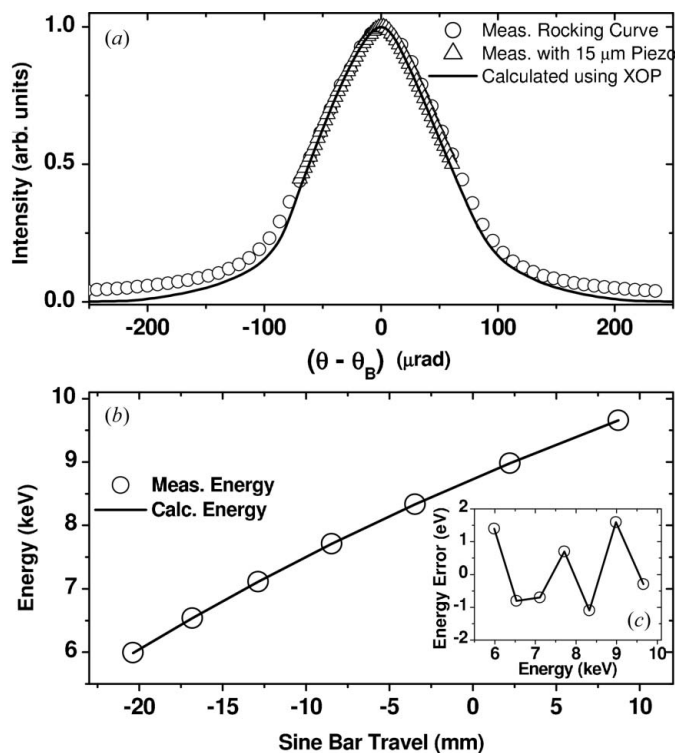


Figure 7 Monochromatic beam from the artificial channel-cut monochromator imaged using a CCD detector, showing a highly improved uniformity in the intensity distribution compared with that from the traditional channel-cut shown in Figs. 1(a)–1(c). The intensity cross section measured using a $20 \mu\text{m} \times 20 \mu\text{m}$ aperture on a PIN diode point detector (b) in the horizontal and (c) in the vertical direction.

The spectral characterization results of the artificial channel-cut monochromator are shown in Fig. 8. Fig. 8(a) shows the rocking curve measured by rotating the second Ge(111) crystal across the Bragg peak relative to the first Ge(111) crystal, using the picomotor as well as the piezo actuator. The limited $15 \mu\text{m}$ travel range of the piezo actuator allowed measurement of the rocking curve to the full width at half-maximum, whereas the picomotor allowed the measurement of the complete rocking curve. It can be seen from Fig. 8(a) that the measured rocking curve is in excellent agreement with the calculations based on the dynamical theory of X-ray diffraction indicating that the crystals are perfect and strain-free. In order to perform an absolute energy calibration, *K*-edge absorption measurements were carried out using seven different metal foils covering an energy range of 6–10 keV. Fig. 8(b) shows the monochromatic photon energy derived from the absorption-edge measurements and the energy calculated from the linear travel of the sine-bar based on the design parameters. The error in the absolute energy, defined as the difference in the measured and calculated monochromatic photon energy, was found to be less than ± 2 eV over the energy range 6–10 keV (Fig. 8c), with no measurable hysteresis. Further, the two crystals once aligned parallel to each other at one energy remained perfectly parallel over the entire energy range. This was verified from


Figure 8

Spectral characterization results from the artificial channel-cut monochromator. (a) Measured and calculated rocking curve. (b) Monochromatic photon energy derived from absorption-edge measurements (open circles), and energy calculated (solid line) based on design parameters plotted against linear travel of the sine bar. (c) Absolute error in the energy (open circles) at different photon energies.

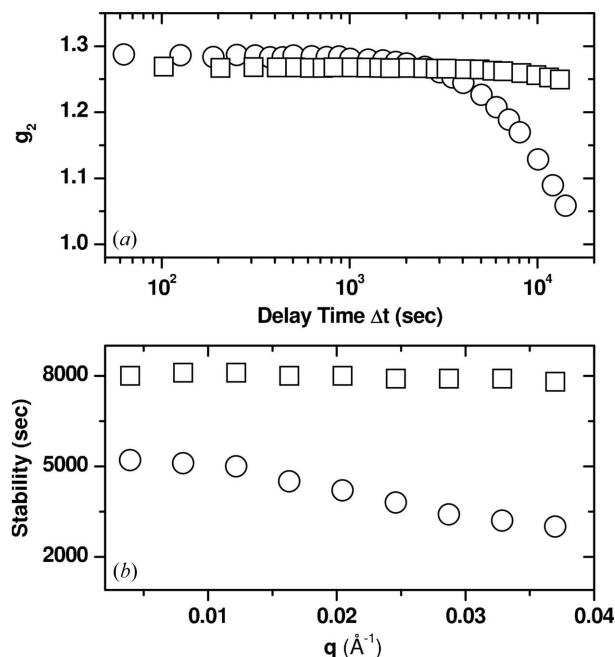
rocking scans made using the piezo actuator at the above energies.

XPCS measurements on a statically disordered aerogel sample were performed to test the stability of the monochromator. XPCS measures the intensity autocorrelation function $[g_2(q, t)]$ defined as

$$g_2(q, t) = \frac{\langle I(q, t')I(q, t' + t) \rangle}{\langle I(q, t') \rangle^2}, \quad (1)$$

where $I(q, t')$ is the scattered intensity at wavevector q and time t' , and $\langle \dots \rangle$ signify an ensemble average over different speckles at the same q and over t' . $g_2(q, t)$ is related to the dynamic structure factor $S(q, t)$ or the normalized intermediate scattering function (ISF) $[f(q, t)]$ via $g_2(q, t) = 1 + A[f(q, t)]^2$, where A is the speckle contrast (Sandy *et al.*, 1999). The aerogel sample is used as a standard for testing the stability of the beamline as the ISF from the aerogel should be static at all time and length scales. Thereby, any decay or roll-off in the measured ISF can be attributed to instability in the beam owing to beamline optics, for example.

Fig. 9(a) shows the time autocorrelation function (g_2) from the aerogel sample measured using the traditional channel-cut and the artificial channel-cut monochromators, at a wavevector transfer (q) of 0.4 nm^{-1} . The roll-off in g_2 at longer measurement times, which is significantly more in the case of the traditional channel-cut monochromator, is attributed to


Figure 9

(a) Time autocorrelation function from a statically disordered aerogel sample measured using the traditional channel-cut (open circles) and artificial channel-cut (open squares) monochromators at wavevector transfer $q = 0.4 \text{ nm}^{-1}$. (b) Time stability limit of the experimental set-up as a function of wavevector transfer q measured using the traditional channel-cut (open circles) and artificial channel-cut (open squares) monochromators.

instabilities in the experimental set-up and inhomogeneities in the beam. We define a time stability limit of the set-up as the fitted location of the roll-off in g_2 at that q . Fig. 9(b) shows the time stability limit measured as a function of q for the traditional channel-cut and the artificial channel-cut monochromators. It can be observed that the stability at larger wavevector transfers (shorter length scales, given by $2\pi/q$) are more sensitive to the instability and inhomogeneity in the beam. Thereby, the artificial channel-cut monochromator, which produces a highly uniform intensity distribution in the beam [Figs. 7(a)–7(c)], contributes to the excellent stability, to very short length scales ($\sim 10 \text{ nm}$).

7. Conclusions

We have designed and successfully implemented an artificial channel-cut monochromator to deliver stable and maximally brilliant monochromatic X-ray beam to XPCS experiments performed at APS beamline 8-ID-I. A novel in-vacuum sine-bar is employed for the combined pitch motion of the two crystals, and flexures are used for aligning the two crystals to the precision of a traditional channel-cut crystal. The artificial channel-cut monochromator delivers an exceptionally uniform beam that directly contributes to enhanced measurement stability and to improved X-ray beam brilliance preservation, both of which proportionally increase the signal-to-noise ratio for XPCS measurements and, consequently, the range of sample dynamics that can be probed. Aside from its

proven utility for XPCS measurements, the monochromator should also be very well suited for 'quick' XANES/EXAFS (Caliebe *et al.*, 2006) and microdiffraction (Ice *et al.*, 2000) type experiments provided that a downstream beam-defining vertical aperture selects a small portion of the beam relative to both the beam size and its vertical displacement with energy. Further, the sine-bar driven by the nanomotion stage can be operated at very high dynamic speeds with a very high repeatability and this has been tested to 0.5 keV s^{-1} with reproducibility within the energy resolution.

A significant portion of the construction costs of the monochromator was provided by an APS X-ray Operations and Research Beamline Competition Award that we gratefully acknowledge. We thank Professors Mark Sutton, Simon Mochrie and Larry Lurio for valuable discussions, and Mark Beno and Thomas Toellner for constructive evaluation of the design. We appreciate the expert technical assistance of D. Nocher, H. Gibson, M. Muscia and R. Ranay, and thank Ruben Khachatryan, Jun Qian and Jozef Maj for optics fabrication, metrology and topography characterization. We are grateful to Bryan Sheldon, Nadir Nimrod, Aaron Dietrich, Evan Reed, Ernie Ponce and Bill Hennessey for their help with the nanomotion stage and ACS motion control system. Use of the APS was supported by the US Department of Energy, Office of Science, Office of Basic Energy Sciences, under contract No. DE-AC02-06CH11357.

References

- Barraza, J., Shu, D. & Kuzay, T. M. (1994). *Nucl. Instrum. Methods A*, **347**, 591–597.
- Caliebe, W. A., So, I., Lenhard, A. & Siddone, D. P. (2006). *Radiat. Phys. Chem.* **75**, 1962–1965.
- Davey, C. (1997). Accelerator Technical Update, ANL/APS/TB-18. Advanced Photon Source, Argonne National Laboratory, IL, USA.
- Falus, P., Borthwick, M. A., Narayanan, S., Sandy, A. R. & Mochrie, S. G. J. (2006). *Phys. Rev. Lett.* **97**, 066102.
- Falus, P., Lurio, L. B. & Mochrie, S. G. J. (2006). *J. Synchrotron Rad.* **13**, 253–259.
- Fluerasu, A., Sutton, M. & Dufresne, E. M. (2005). *Phys. Rev. Lett.* **94**, 055501.
- Gutt, C., Ghaderi, T., Chamard, V., Madsen, A., Seydel, T., Tolan, M., Sprung, M., Grubel, G. & Sinha, S. K. (2003). *Phys. Rev. Lett.* **91**, 076104.
- Ice, G. E., Chung, J. S., Lowe, W., Williams, E. & Edelman, J. (2000). *Rev. Sci. Instrum.* **71**, 2001–2004.
- Li, Y., Khounsary, A., Narayanan, S., Macrander, A., Khachatryan, R. & Lurio, L. B. (2004). *Proc. SPIE*, **5537**, 171–176.
- Lurio, L. B., Lumma, D., Sandy, A. R., Borthwick, M. A., Falus, P., Mochrie, S. G. J., Pelletier, J. F., Sutton, M., Regan, L., Malik, A. & Stephenson, G. B. (2000). *Phys. Rev. Lett.* **84**, 785–788.
- Narayanan, S., Sandy, A. R., Sprung, M., Sullivan, J., Preissner, C. & Shu, D. (2006). *Proceedings of the Ninth International Conference on Synchrotron Radiation Instrumentation*, edited by J.-Y. Choi and S. Rah, *AIP Conference Proceedings 879*, pp. 911–914. New York: American Institute of Physics.
- Pfeifer, M. A., Williams, G. J., Vartanyants, I. A., Harder, R. & Robinson, I. K. (2006). *Nature (London)*, **442**, 63–66.
- Sandy, A. R., Lurio, L. B., Mochrie, S. G. J., Malik, A., Stephenson, G. B., Pelletier, J. F. & Sutton, M. (1999). *J. Synchrotron Rad.* **6**, 1174–1184.
- Shu, D., Toellner, T. S. & Alp, E. E. (2000). *Proceedings of the Eleventh US National Conference on Synchrotron Radiation Instrumentation*, edited by P. Pianetta, *AIP Conference Proceedings 521*, pp. 219–224. New York: American Institute of Physics.
- Shu, D., Toellner, T. S. & Alp, E. E. (2003). US Patent 6 607 840.
- Shu, D., Toellner, T. S., Alp, E. E., Maser, J., Ilavsky, J., Shastri, S. D., Lee, P. L., Narayanan, S. & Long, G. G. (2007). *Proceedings of the Ninth International Conference on Synchrotron Radiation Instrumentation*, edited by J.-Y. Choi and S. Rah, *AIP Conference Proceedings 879*, pp. 1073–1076. New York: American Institute of Physics.
- Shu, D., Yun, W., Lai, B., Barraza, J. & Kuzay, T. M. (1995). *Rev. Sci. Instrum.* **66**, 1786–1788.
- Vartanyants, I. A. & Robinson, I. K. (2003). *Opt. Commun.* **22**, 29–50.
- Wang, Y., Xiao, T. & Xu, H. (2000). *J. Synchrotron Rad.* **7**, 209–214.
- Williams, G. J., Pfeifer, M. A., Vartanyants, I. A. & Robinson, I. K. (2003). *Phys. Rev. Lett.* **90**, 175501.